Combined numerical and experimental study of microstructure and permeability in porous granular media

Philipp Eichheimer[1], Marcel Thielmann[1], Wakana Fujita[2], Gregor J. Golabek[1], Michihiko Nakamura[2], Satoshi Okumura[2], Takayuki Nakatani[2], and Maximilian O. Kottwitz[3]

[1]Bayerisches Geoinstitut, University of Bayreuth, Universitätsstrasse 30, 95447 Bayreuth, Germany
[2]Department of Earth Science, Tohoku University, 6-3, Aramaki Aza-Aoba, Aoba-ku, Sendai 980-8578, Japan
[2]Institute of Geoscience, Johannes Gutenberg University, Johann-Joachim-Becher-Weg 21, 55128 Mainz, Germany

Correspondence: Philipp Eichheimer (Philipp.Eichheimer@uni-bayreuth.de)

Abstract. Fluid flow on different scales is of interest for several Earth science disciplines like petrophysics, hydrogeology and volcanology. To parameterize fluid flow in large-scale numerical simulations (e.g. groundwater and volcanic systems), flow properties on the microscale need to be considered. For this purpose experimental and numerical investigations of flow through porous media over a wide range of porosities are necessary. In the present study we sinter glass bead media with various porosities. The microstructure, namely effective porosity and effective specific surface, is investigated using image processing. We determine flow properties like hydraulic tortuosity and permeability using both experimental measurements and numerical simulations. By fitting microstructural and flow properties to porosity, we obtain a modified Kozeny-Carman equation for isotropic low-porosity media, that can be used to simulate permeability in large-scale numerical models. To verify the modified Kozeny-Carman equation we compare it to the computed and measured permeability values.

1 Introduction

The understanding of transport and storage of geological fluids in sediments, crust and mantle is of major importance for several Earth science disciplines including volcanology, hydrology and petroleum geoscience (Manwart et al., 2002; Ramandi et al., 2017; Honarpour, 2018). In volcanic settings melt segregation from partially molten rocks controls the magma chemistry, and outgassing of magmas influences both magma ascent and eruption explosivity (Collinson and Neuberg, 2012; Lamur et al., 2017; Mueller et al., 2005). In hydrogeology fluid flow affects ground water exploitation and protection (Domenico and Schwartz, 1998; Hölting and Coldewey, 2019), whereas in petroleum geoscience fluid flow controls oil recovery efficiency (Suleimanov et al., 2011; Hendraningrat et al., 2013; Zhang et al., 2014).

A key parameter for fluid flow is permeability. Permeability estimations have been performed on several scales ranging from pore scale (Brace, 1980) to macroscale (Fehn and Cathles, 1979; Norton and Taylor Jr, 1979). As the permeability on the macroscale is a function of its microstructure it is necessary to accurately predict permeability based on microscale properties (Mostaghimi et al., 2013). To achieve this goal, various experimental and numerical approaches have been developed over the years (e.g. Keehm, 2003; Andrä et al., 2013a; Gerke et al., 2018; Saxena et al., 2017).

Assuming laminar flow (Bear, 1988; Matyka et al., 2008), flow through porous media can be described using Darcy's law (Darcy, 1856), which relates the fluid flux Q to an applied pressure gradient ΔP

$$Q = -\frac{k}{\eta}\Delta P, \tag{1}$$

where k is the permeability and η the fluid viscosity. A first simple capillary model for the permeability of a porous media was proposed by Kozeny (1927)

$$k = k_0 \frac{\phi^3}{S^2}, \tag{2}$$

where k_0 is the dimensionless Kozeny constant depending on the channel geometry (e.g. $k_0 = 0.5$ for cylindrical capillaries), ϕ

30 is the porosity and S is the specific surface area (ratio of exposed surface area to bulk volume). Later this relation was extended by Carman (1937, 1956), investigating the fluid flow through a granular bed, taking its microstructure into account. For this purpose Carman (1937, 1956) introduced the term tortuosity, being the ratio of effective flow path L_e to a straight path L.

$$\tau = \frac{L_e}{L} \tag{3}$$

Introducing this relation into eq.(2) leads to the well-known Kozeny-Carman equation:

35
$$k = k_0 \frac{\phi^3}{\tau^2 S^2}, \tag{4}$$

Using experimental data Carman (1956) determined that tortuosity τ is $\approx \sqrt{2}$. The Kozeny-Carman equation was derived assuming that the medium consists only of continuous, curved channels with constant cross-section (Carman, 1937; Bear, 1988). However, in porous media pathways most likely do not obey these assumptions and therefore applying this equation to porous media remains challenging and in some cases fails for low porosities (Bernabe et al., 1982; Bourbie et al., 1992) or mixtures of

40 different shapes and material sizes (Carman, 1937; Wyllie and Gregory, 1955). This has led to modifications and extensions of the Kozeny-Carman equation and its parameters. For instance Mavko and Nur (1997) extended the Kozeny-Carman equation by considering a percolation threshold porosity ϕ_c, below which no continuous pathways exist. Additional modifications have been made to account for correlations between tortuosity, specific surface and porosity (Comiti and Renaud, 1989; Pech, 1984; Mota et al., 2001; Pape et al., 2005). These studies either use experimental, analytical or numerical approaches for mostly two

45 dimensional porous media with porosities $> 30\%$. Here, we fit correlations for three dimensional nearly isotropic spherical media in the low porosity regime ($< 22\%$), which can be compared to sandstones.

Since the ascent of Digital Rock Physics (DRP) it has become viable to study microstructures of porous media in more detail using micro Computed Tomography (micro-CT) and Nuclear Magnetic Resonance (NMR) images (Arns et al., 2001; Arns, 2004; Dvorkin et al., 2011). Using these images it is possible to compute fluid flow and several microstructural properties like

50 porosity and specific surface as well as fluid properties including tortuosity and permeability. For this purpose several numerical methods including Finite Elements (FEM), Finite Differences (FDM) and Lattice Boltzmann method (LBM) (Saxena et al., 2017; Andrä et al., 2013a; Gerke et al., 2018; Shabro et al., 2014; Manwart et al., 2002; Bird et al., 2014) can be used.

Parameterizing those microstructural and fluid flow properties, which can be used as input for large-scale numerical models requires systematic data sets. Yet, very few data sets exist that investigate microstucture (porosity and specific surface) and related flow parameters (tortuosity and permeability) using systematically sintered samples $< 22\%$ porosity. Most of the previous studies either measure permeability experimentally without investigating its microstructure or compute permeability and related microstructural parameters, but can not compare to experimental data sets as structural images are not available. For this reason we sinter isotropic porous glass bead samples with porosities ranging from $1.5\% - 22\%$, representing sedimentary rocks up to a depth of ≈20 km (Bekins and Dreiss, 1992). The microstructure is investigated using image processing. Permeability is measured experimentally using a permeameter (see sec.2.2; Takeuchi et al. (2008); Okumura et al. (2009)) and numerically using the finite difference code LaMEM (see sec.2.5; Kaus et al. (2016); Eichheimer et al. (2019)). Theoretical permeability predictions (eq.(4)) require three input parameters, namely porosity, specific surface and hydraulic tortuosity. Within this study these parameters are determined and related to the porosity. Thus, we are able to provide a modified Kozeny-Carman equation depending on porosity only.

2 Methods

Here we first describe the experimental workflow including sample sintering and permeability measurement, followed by the numerical workflow featuring image processing, computation of fluid velocities and determination of both hydraulic tortuosity and permeability. Fig.1 shows an overview of the entire workflow which will be explained in detail in the following section.

2.1 Sample sintering

Glass bead cylinders with different porosities were sintered under experimental conditions as summarized in Table 1. For this purpose soda-lime glass beads with diameters ranging from 0.9 to 1.4 mm were utilized as starting material (see grain size distribution in sec.B). For each sample, we prepared a graphite cylinder with 8.0 mm inner diameter and ≈10 mm height. Additional samples with diameters of 10 and 14 mm were prepared to check for size effects (see tab.1). At the bottom of the graphite cylinder a graphite disc (11.5 mm diameter and 3.0 mm thick) was attached using a cyanoacrylate adhesive (see fig.2 inset). The glass beads were poured into the graphite cylinder and compressed with steel rods (8-14 mm diameter) before heating.

The glass bead samples were then sintered in a muffle furnace at $710\,^{\circ}$C under atmospheric pressure. The temperature of $710\,^{\circ}$C was found to be suitable for sintering of the glass beads as it is slightly below the softening temperature of soda-lime glass around $720 - 730\,^{\circ}$C (Napolitano and Hawkins, 1964) and well above the glass transition temperature of soda-lime glass at $\approx550\,^{\circ}$C (Wadsworth et al., 2014). At $710\,^{\circ}$C the viscosity of the employed soda-lime glass is on the order of $10^7\,\mathrm{Pas}$ (Kuczynski, 1949; Napolitano and Hawkins, 1964; Wadsworth et al., 2014) allowing for viscous flow of the glass beads at their contact surface driven by surface tension. Using different time spans ranging from $60 - 600$ minutes the viscous flow at $710\,^{\circ}$C controls the resulting porosity of the sample.

Workflow to experimentally and numerically determine permeability of porous glass samples
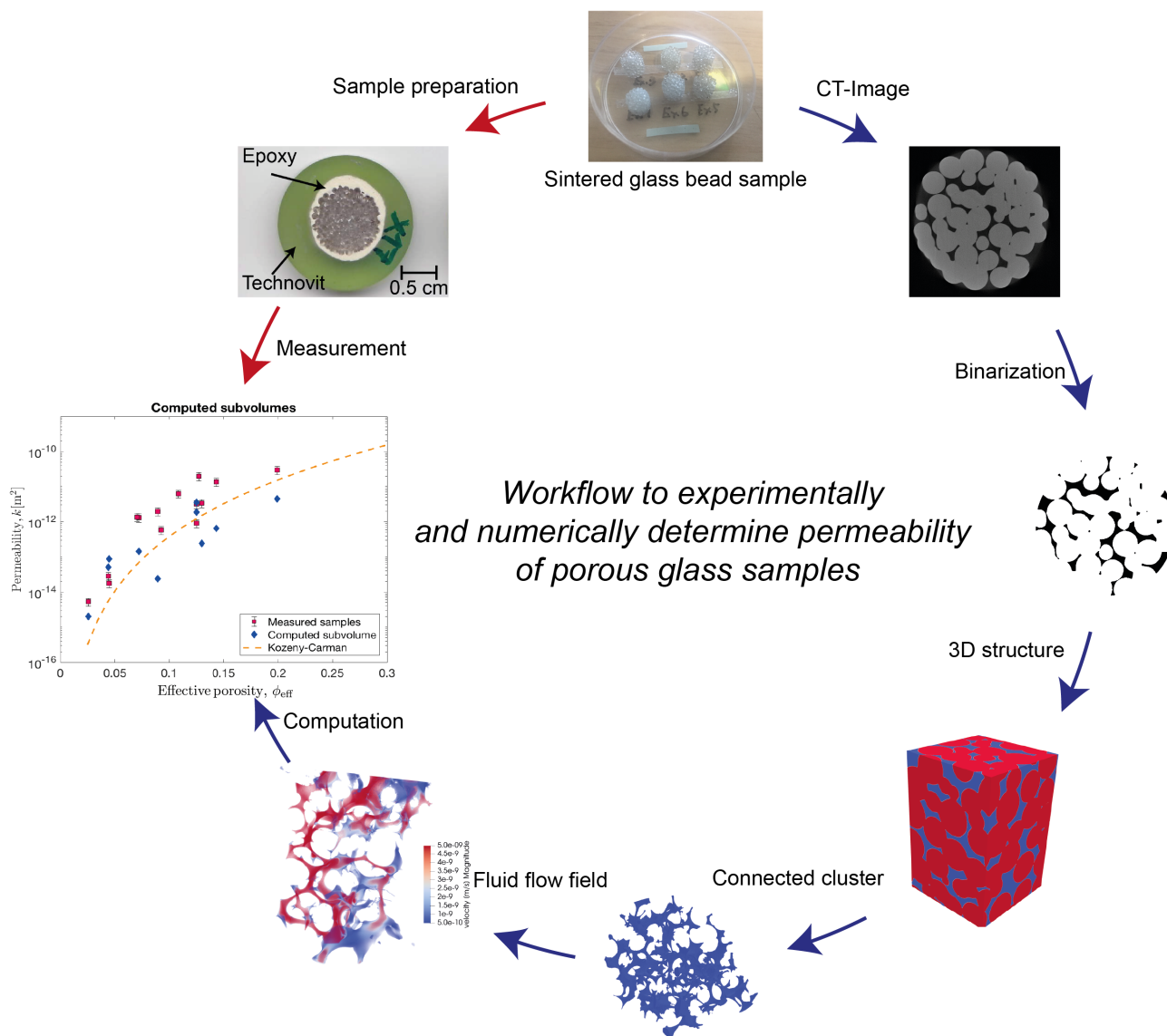
Figure 1. Workflow process map - red arrows mark the experimental workflow, whereas blue arrows indicate the numerical workflow.

After sintering, the sample was cooled down to $550 - 600\,°C$ within ≈ 5 minutes. Afterwards the sample was taken out of

85   the furnace to adjust to room temperature to prevent thermal cracking of the sample. In a next step the graphite container was removed from the sample. It should be noted that during the process of sintering gravity slightly affects the porosity distribution within the glass bead sample (see fig.2). However, the subsamples used to compute the numerical permeability do not cover the whole height of the sample, thus the effect of compaction on the results is limited.
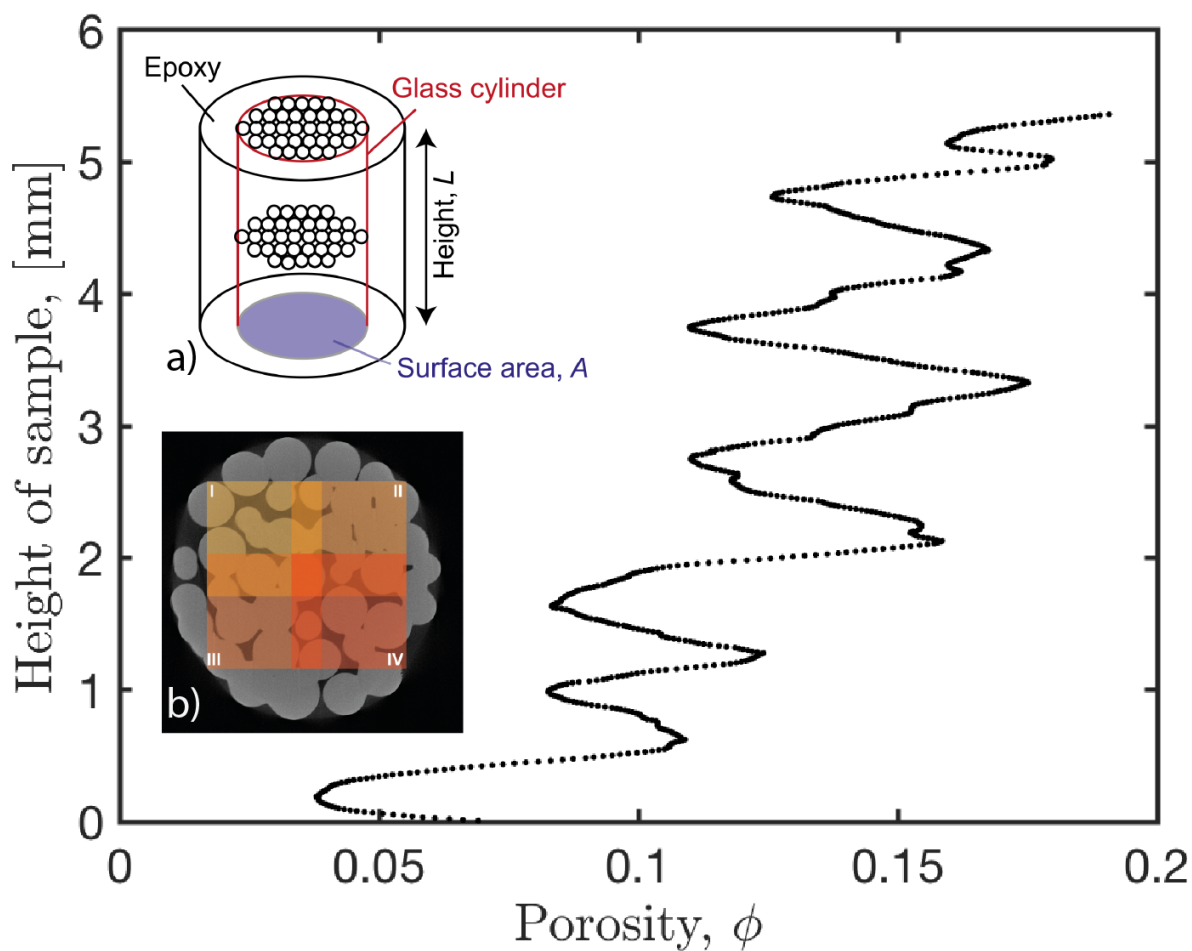
Figure 2. Computed porosity of each CT-slice from top to the bottom of a full sample (z-axis; sample Ex14). The diagram shows that gravity affects the porosity of the sample. Porosity minima correspond to distinct layers of glass bead within the sample. The inset **a)** provides a sketch of the sample structure. In the inset the red color outlines the cylindrical shape, blue the surface area A of the cylinder and L the height of the sample. **b)** shows chosen locations for the squared subsamples 1-4. Additional four subsamples (5-8) are placed similarly below subsamples 1-4 overlapping in z-direction.

2.2 Experimental permeability measurement

90   In a first preparation step we wrap a highly viscous commercial water resistant resin around the sample to avoid pore space infiltration. In a next step we embed the sample within a less viscous resin (Technovit 4071, Heraeus Kulzer GmbH & Co. or Presin, Nichika Inc.) to create an airproof casing. The upper and lower surface of the sample were grinded and polished to prevent leaks during experimental permeability measurements (fig.1; Sample preparation).

The experimental permeability measurements were conducted at Tohoku University using a permeameter, described in
95   Takeuchi et al. (2008) and Okumura et al. (2009). To determine the permeability the air flow through a sample is measured at
room temperature. The pressure gradient between sample inlet and outlet is controlled by a pressure regulator (RP1000-8-04,
CKD Co.; Precision $\pm 0.1\,\%$) at the inlet side. To monitor the pressure difference a digital manometer (testo526-s, Testo Inc.;
Precision $\pm 0.05\,\%$) is used. Air flow through the sample is measured using a digital flow meter (Alicat, M-10SCCM; Precision
$\pm 0.6\%$). As Darcy's law assumes a linear relationship between the pressure and flow rate, we measure the gas flow rate at
100   several pressure gradients (see fig.A1 in Appendix A) to verify our assumption of laminar flow conditions. The permeability
of all samples is calculated using Darcy's law (eq.(1)), the measured values and additional parameters (Tab.1).

Table 1. Experimental parameters of sintering conditions and parameters used to compute permeability using Darcy's law. A denotes the
sample surface area, L the height of the glass bead cylinders, D the inner diameter of each capsule. The sintering time in minutes, the total
weight of the glass beads and the experimentally measured permeability are given. The effective porosity ϕ_{eff} shown here is computed using
image processing (see sec.2.6).

Sample	Porosity ϕ_{tot} (%)	Porosity ϕ_{eff} (%)	Area A (cm^2)	Height L (mm)	Capsule ∅ D (mm)	Time t_{sint} (min)	Tot. weight m (g)	Permeability K_{meas} (m^2)
X02	20.94	20.94	0.438	5.11	8	120	0.574	$(3.1 \pm 0.2) \times 10^{-11}$
X11	6.72	4.75	0.434	3.63	8	180	0.575	$(1.91 \pm 0.09) \times 10^{-14}$
X14	13.28	13.22	0.407	5.12	8	60	0.576	$(3.4 \pm 0.2) \times 10^{-12}$
X15	2.54	1.21	0.412	4.76	8	480	0.575	$(5.7 \pm 0.3) \times 10^{-15}$
X16	6.07	4.50	0.808	5.05	10	120	0.899	$(3.1 \pm 0.2) \times 10^{-14}$
X17	12.90	12.85	1.569	5.18	14	120	1.762	$(1.41 \pm 0.07) \times 10^{-12}$
X29	9.01	8.97	0.441	4.55	8	300	0.576	$(6.3 \pm 0.3) \times 10^{-13}$
X30	7.12	7.03	0.420	4.81	8	600	0.574	$(1.52 \pm 0.08) \times 10^{-12}$
X31	9.92	9.87	0.423	4.73	8	300	0.576	$(2.1 \pm 0.1) \times 10^{-12}$
X32	13.52	13.44	0.342	4.47	8	480	0.576	$(3.7 \pm 0.2) \times 10^{-12}$
X33	15.97	15.96	0.412	4.80	8	180	0.575	$(1.53 \pm 0.08) \times 10^{-11}$
X35	14.17	14.15	0.411	4.78	8	360	0.575	$(2.2 \pm 0.1) \times 10^{-11}$
X36	10.71	10.67	0.372	4.15	8	420	0.575	$(6.9 \pm 0.4) \times 10^{-12}$

2.3   Micro-CT images and segmentation

Before preparing the samples for permeability measurements all samples are digitized using micro Computed Tomographic
scans (micro-CT) performed at Tohoku University (ScanXmate-D180RSS270) with a resolution $\approx 6 - 10\,\mu m$ according to the
105   method of Okumura and Sasaki (2014). Andrä et al. (2013b) showed that the process of segmentation of the micro-CT images
may have a significant effect on the three dimensional pore space and therefore the computed flow field. In two-phase systems
(fluid + mineral), as in this study, the segmentation is straightforward due to the high contrast in absorption coefficients between

glass beads and air, while it can become quite complex for multiphase systems featuring several mineral phases. In the present study the segmentation of the obtained micro-CT images was done using build-in MatLab functions. In a first step the images

110   are binarized using Otsu's method (Otsu, 1979). Additional smoothing steps of the images are performed. In a next step the two dimensional micro-CT slices are stacked on top of each other, resulting in a three dimensional representation of the pore space (fig.1; 3D structure).

As isolated clusters of pore space do not contribute to the permeability, we extract all percolating clusters of pore space using a flooding algorithm (bwconncomp). As a bonus, this procedure reduces the computational cost for numerical permeability

115   determinations by removing irrelevant parts of the pore space.

2.4   Numerical method

The relationship between inertial and viscous forces in fluid flows is described by the Reynolds number:

$$Re = \frac{\rho v L}{\eta}, \tag{5}$$

where ρ is the density, v the velocity component, L denotes the length of the domain and η is the viscosity of the fluid. For

120   laminar flow conditions ($Re < 1$, see fig.A1 Appendix A) and ignoring gravity, the flow in porous media can be described with the incompressible Stokes equations:

$$\frac{\partial v_i}{\partial x_i} = 0 \tag{6}$$

$$\frac{\partial}{\partial x_j} \left[\eta \left(\frac{\partial v_i}{\partial x_j} + \frac{\partial v_j}{\partial x_i} \right) \right] - \frac{\partial P}{\partial x_i} = 0 \tag{7}$$

with P being the pressure and x the spatial coordinate. For all simulations, we employed a fluid viscosity of 1 Pa s.

125   The Stokes equations are solved using the finite difference code LaMEM (Kaus et al., 2016; Eichheimer et al., 2019). LaMEM employs a staggered grid Finite Difference scheme (Harlow and Welch, 1965), where pressures P are defined at the cell centers and velocities v at cell faces. Based on the data from the CT-scans, each cell is assigned either a fluid or a solid phase. The discretized system of equations is then solved using multigrid solvers of the PETSc library (Balay et al., 2019). As only cells within the fluid phase contribute to fluid flow the discretized governing equations are only solved for these cells.

130   This greatly decreases the number of degrees of freedom and therefore significantly reduces the computational cost. Due to computational limitations and the densification at the bottom of the samples (see fig.2) we extract 8 overlapping subvolumes per full sample (see fig.2b), with sizes of 512^3 cells. For each subvolume we compute effective porosity, effective specific surface, hydraulic tortuosity and permeability.

2.5 Numerical permeability computation

135 From the calculated velocity field in z-direction the volume-averaged velocity component v_m is calculated (e.g. Osorno et al., 2015):

$$v_m = \frac{1}{V_f} \int\limits_{V_f} |v_z|\, dv,$$ (8)

where V_f is the volume of the fluid phase. Using Darcy's law (eq.1; Andrä et al., 2013a; Bosl et al., 1998; Morais et al., 2009; Saxena et al., 2017) an intrinsic permeability k_s is computed via:

140 $$k_s = \frac{\eta v_m}{\Delta P}$$ (9)

2.6 Effective porosity

Porosity is an important parameter describing microstructures. It is defined as the ratio of pore space V_V to the bulk volume of the sample V_B (Bird et al., 2006):

$$\phi = \frac{V_V}{V_B}$$ (10)

145 In this study we compute an effective porosity for each sample from its obtained micro-CT data. In our case the effective porosity is defined as the porosity of all percolating clusters of pore space to the total volume of material:

$$\phi_{eff} = \frac{V_{V_{\text{eff}}}}{V_B}$$ (11)

It should be mentioned that in a simple capillary model $\phi_{\text{eff}} = \phi$ since no isolated pore space exists. Further it should be noted that we only use the effective porosity to determine microstructural and flow parameters.

150 2.7 Effective specific surface

The specific surface is defined as the total interfacial surface area of pores A_s per unit bulk volume V_b of the porous medium (Bear, 1988):

$$S = \frac{A_s}{V_b}$$ (12)

As in the previous section we compute the effective specific surface of all percolating clusters of pore space and neglect isolated
155 pore space.

2.8 Hydraulic tortuosity

In recent years several definitions for hydraulic tortuosity have been suggested (Clennell, 1997; Bear, 1988; Ghanbarian et al., 2013). Numerically Matyka et al. (2008) determined the hydraulic tortuosity by using an arithmetic mean given as:

$$\tau_h = \frac{1}{N} \sum_{i=1}^{N} \tau(r_i),$$ (13)

160   where $\tau = L_e/L$ is the tortuosity of a flow line crossing through point r_i (eq.(3)) and N the total number of streamlines.

Koponen et al. (1996) computed the tortuosity numerically using:

$$\tau_h = \frac{\sum_i \tau^n(r_i)v(r_i)}{\sum_i v(r_i)}, \tag{14}$$

where $v(r_i) = |v(r_i)|$ is the fluid velocity at point r_i and points r_i are chosen randomly from the pore space (Koponen et al., 1996).

165   Both numerical and experimental studies published different relations of hydraulic tortuosity to porosity. One of the most common relations for hydraulic tortuosity is a logarithmic function of porosity reading as follows:

$$\tau_h(\phi) = 1 - Bln(\phi), \tag{15}$$

where B is a constant found experimentally for different particles (e.g. 1.6 for wood chips Pech (1984); Comiti and Renaud (1989), 0.86 to 3.2 for plates Comiti and Renaud (1989)). By numerically computing hydraulic tortuosity for two dimen-

170   sional squares, Matyka et al. (2008) obtained $B = 0.77$. A different experimental relation for tortuosity measuring the electric conductivity of spherical particles was proposed by Mota et al. (2001):

$$\tau_h(\phi) = \phi^{-0.4} \tag{16}$$

Investigating two-dimensional porous media with rectangular shaped particles Koponen et al. (1996) proposed a different relation:

175   $$\tau_h(\phi) = 1 + 0.8(1 - \phi) \tag{17}$$

It should be mentioned that the tortuosity-porosity relations stated above mostly have been obtained for porous media with $> 30\%$ porosity.

In the present study the hydraulic tortuosity is determined according to eq.(13). To compute the hydraulic tortuosity pathways τ for each sample need to be computed. Pathways describe a curve traced out in time by a fluid particle with fixed mass and

180   reads mathematically as

$$\frac{\partial x_i}{\partial t} = v(x,t), \tag{18}$$

with v being the computed velocity field obtained from the numerical simulation and t being the time. Integrating eq.(18) yields

$$x_i = x_i(x^0, t), \tag{19}$$

185   where x^0 is the position of the prescribed particle at $t = 0$. Eq.(18) is solved using built-in MatLab ODE (Ordinary Differential Equation) solvers. To compute the pathway length all fluid cells at the inlet of the subsample are extracted. Using the computed velocity field and eq.(18) the pathway length for each extracted fluid cell is calculated. Hence, up to 40000 pathways needs to be computed for a subsamples with $\approx 20\%$ porosity, whereas for a subsamples with $\approx 5\%$ porosity up to 5000 pathways are computed. The resulting length of each pathway is used to compute the hydraulic tortuosity according to eq.(13).

190 ## 3 Results

In this section we present results on microstructural properties like effective specific surface and flow properties like hydraulic tortuosity and permeability. All data for each subsample presented here are given in the supplementary tables. Effective porosity and effective specific surface are computed for both subsamples and full samples, whereas hydraulic tortuosities and permeability are only computed for the subsamples due to computational limitations.

195 ### 3.1 Effective specific surface

Figure 3 shows the computed specific surfaces for all subsamples and all full samples with increasing effective porosity. Koponen et al. (1997) used the following relationship to predict the specific surface:

$$S = -\frac{n}{R_0}\phi_{\mathrm{eff}}ln(\phi_{\mathrm{eff}}), \tag{20}$$

where n is the dimensionality and R_0 is the hydraulic radius of the particles. To relate the computed values for the effective
200 specific surface to the effective porosity the above equation is fitted, resulting in a hydraulic radius of $385.09\,\mu m$. The fit between eq.(20) and our data shows good agreement expressed in terms of the R^2 parameter, representing to which extent a fit represents the data points, equal to 0.975 (see fig.3). Thus our fit of effective specific surface to effective porosity reads as follows:

$$S(\phi_{\mathrm{eff}}) = -\frac{3}{3.8509 \times 10^{-4}\,m}\phi_{\mathrm{eff}}ln(\phi_{\mathrm{eff}}) \tag{21}$$

205

3.2 Hydraulic tortuosity

Figure 4 compares different hydraulic tortuosity-porosity relations presented in section 2.8 to our data. Figure 4a) shows the published porosity-tortuosity relation from Matyka et al. (2008) (see eq.(15)) represented by a dashed black line. The fitted relation is given by a red line with corresponding 95% confidence bounds. Figure 4b) displays the hydraulic tortuosity-porosity
210 relations proposed by Koponen et al. (1996) (see eq.(17)) symbolized by the dashed black line and in yellow our fit to the computed hydraulic tortuosity. Additionally figure 4c) presents the relation of Mota et al. (2001) (see eq.(16)). It should be noted that hydraulic tortuosities in figure 4a, c and d are computed according to eq.(13), whereas tortuosities in figure 4b are computed using eq.(14). As can be seen in figure 4a-c our computed hydraulic tortuosities do not agree well with the models suggested by previous studies. The R^2 values for these fits are either negative or quite small, which shows that the
215 arithmetic mean is an equivalent good fit. Apart from some scattering, our hydraulic tortuosity values appear to be almost constant independent of the effective porosity. The computed hydraulic tortuosities of the present study can be fitted using the following equation plotted in figure4d:

$$\tau_h(\phi_{\mathrm{eff}}) = -0.8712\phi_{\mathrm{eff}} + 3.021 \tag{22}$$

The figure shows a plot with the following annotations:

$$S = -\frac{3}{R_0}\phi_{\text{eff}}\,ln(\phi_{\text{eff}}); \quad R_0 = 385.09 \ \mu m$$

$$R^2 = 0.975$$

Axis labels: Effective specific surface, μm^{-1} (y-axis, $\times 10^{-3}$); Effective porosity, ϕ_{eff} (x-axis)

Legend:
▲ This study - subsamples
■ This study - full samples
— This study - fit
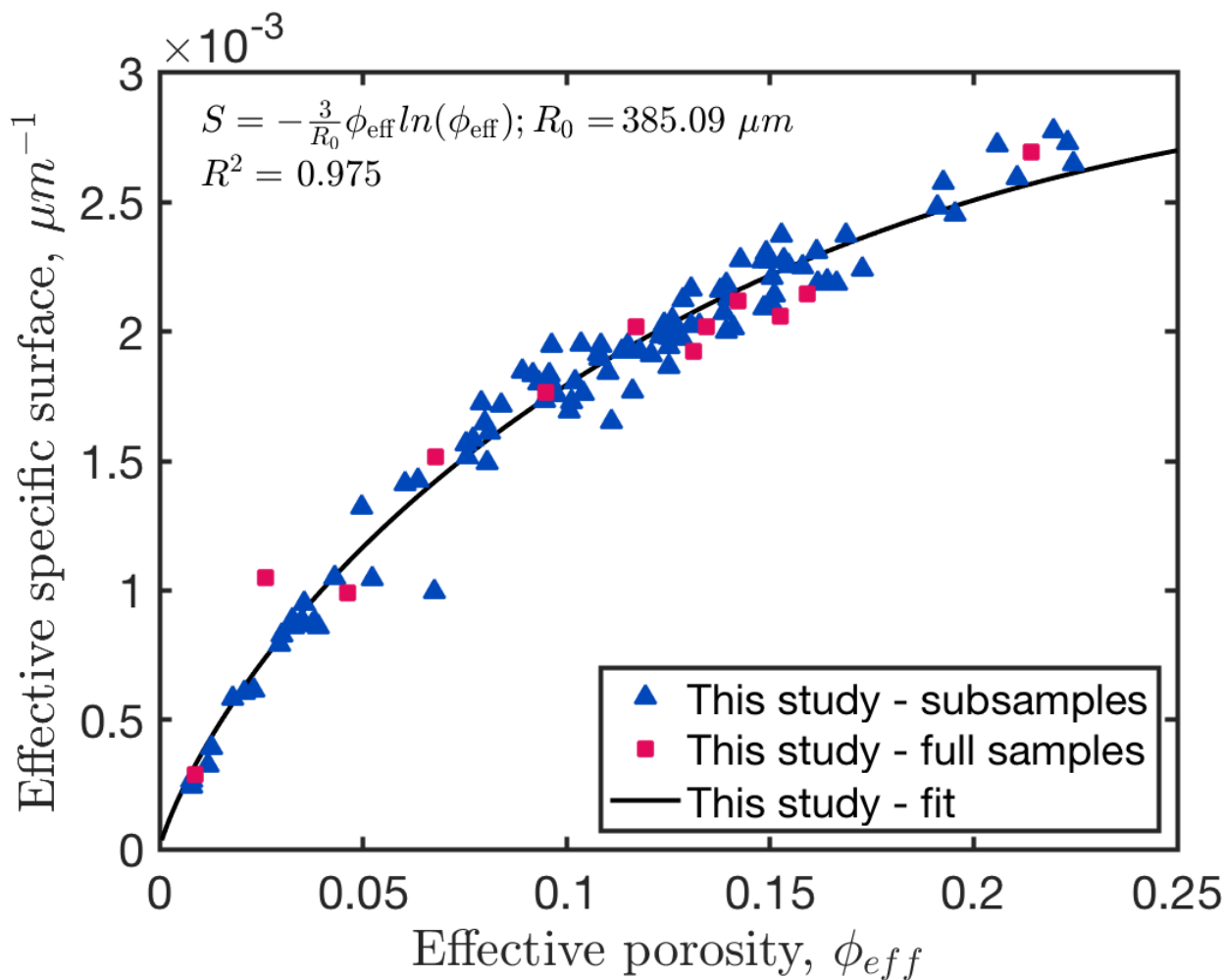
Figure 3. Effective specific surface as a function of effective porosity. Blue triangles represent subsample data from this study and red squares the effective specific surface of full samples. Full sample data points are plotted in order to show that in terms of effective specific surface subsamples represent full samples very well. The black curve represents the fitted curve according to eq.(21).

Yet, this fit does not represent a good correlation, represented by a low R^2 value. We therefore use both the arithmetic mean
220   and eq.(22) for later theoretical permeability predictions. The relatively constant tortuosity, in contrast with many previous models in which tortuosity increases with decreasing porosity, shows that the pore distribution of our experimental products is homogeneous and the geometrical similarity of pore structure was kept during sintering.
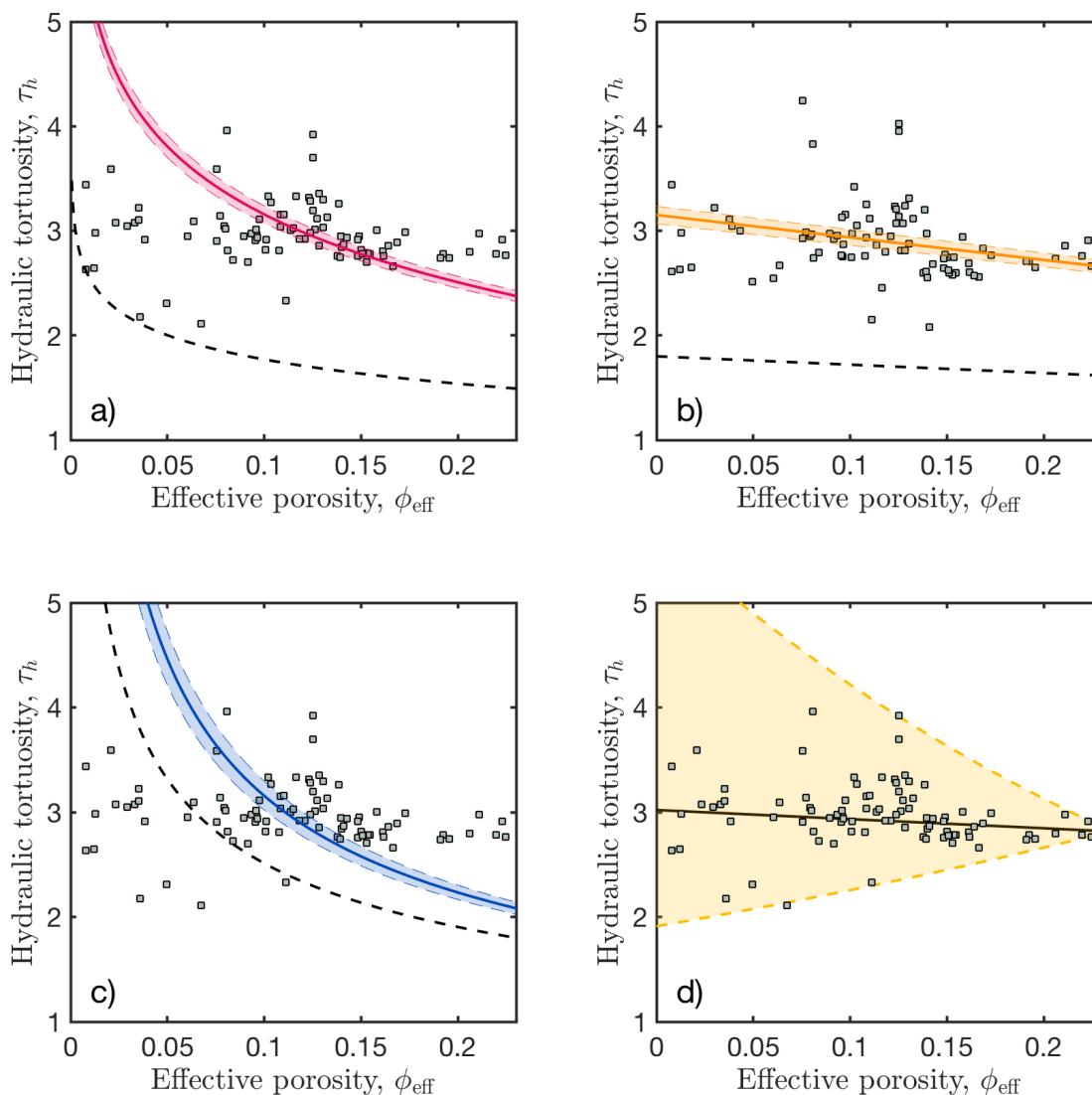
Figure 4. (a)-(c) show the proposed relations for the hydraulic tortuosity according to **(a)** Matyka et al. (2008), **(b)** Koponen et al. (1996) and **(c)** Mota et al. (2001) as black dashed lines. The colored solid lines represent the fit of the computed data to those relations within the 95% confidence bounds. Hydraulic tortuosities for all subsamples (grey squares) are computed according to the method used in each of these studies. **(d)** shows the fit found in the present study. The colored area in **(d)** illustrates the extending distribution of computed hydraulic tortuosities with decreasing effective porosity.

3.3 Permeability prediction

To predict the permeability of the respective samples, the expressions for effective specific surface and hydraulic tortuosity are
225 inserted into the Kozeny-Carman equation (eq.(4)):

$$k = k_0 \frac{(\phi_{\text{eff}} - \phi_{\text{c}})^3}{\tau(\phi_{\text{eff}})^2 S(\phi_{\text{eff}})^2} \tag{23}$$

with $k_0 = 0.5$ being the geometrical parameter for spherical particles (Kozeny, 1927) and $\phi_c = 0.015$ as the critical porosity
threshold based on the lowest effective porosity of a subsample from our study showing a continuous pathway. The critical
porosity threshold ϕ_c in this study is lower than the value of $\phi_c = 0.03$ calculated by previous studies (Van der Marck, 1996;
230 Rintoul, 2000; Wadsworth et al., 2016) and is related to the formation of dead-ends during sintering (see Appendix D).

As the fit for hydraulic tortuosity is not very good, we additionally use the arithmetic mean of all computed hydraulic
tortuosities as input for eq.(23). Using eq.(22) the parameterization for permeability reads:

$$k = k_0 \frac{(\phi_{\text{eff}} - \phi_{\text{c}})^3}{[(-0.8712\phi_{\text{eff}}) + 3.021]^2 \cdot \left[-\frac{3}{3.8509 \times 10^{-4} \, m} \phi_{\text{eff}} ln(\phi_{\text{eff}}) \right]^2}, \tag{24}$$

Furthermore only using the arithmetic mean the parameterization denotes:

235 $$k = k_0 \frac{(\phi_{\text{eff}} - \phi_{\text{c}})^3}{2.9715^2 \cdot \left[-\frac{3}{3.8509 \times 10^{-4} \, m} \phi_{\text{eff}} ln(\phi_{\text{eff}}) \right]^2}, \tag{25}$$

To assess the predictive power of this parameterization, we compare the predictions made by eq.(24) and eq.(25) to both ex-
perimentally and numerically determined permeabilities (fig. 5). The permeability estimation lies in between measured and
computed values for permeability. While experimentally determined permeability values yield towards lower permeabilities,
computed permeabilities tend to lie above the estimation obtained from the Kozeny-Carman equation. In particular, for very
240 low porosities the computed values differ from the permeability prediction. Furthermore values for some computed subsam-
ples are several orders of magnitude higher than the theoretical permeability predictions. As some of the subsamples do not
feature continuous pathways, we compute the geometric mean of the permeability based on the results for all 8 subsamples
(fig.5; inset). For this purpose we assume $k = 10^{-20} \, \text{m}^2$ for subsamples without continuous pathways, referring to a nearly
impermeable medium. The geometric mean shows that the computed permeabilities approach both the Kozeny-Carman curve
245 and the measured permeabilities.

As discussed by previous studies the accuracy of permeability prediction improves with increasing numerical resolution
(Gerke et al., 2018; Keehm, 2003; Eichheimer et al., 2019). To investigate this effect with respect to our samples, we computed
the permeability of two subsamples (Ex35_04 & Ex36_02 see supplement material) using an increased resolution of 1024^3
grid points. The two samples with effective porosities at around 9 and 15% represent samples on both sides of the median of
250 the present study's effective porosity range ($1.5 - 22\%$). The permeability obtained using doubled grid resolution decreases
only by around $\approx 2 - 4\%$ compared to the outcome of models with 512^3 grid resolution (see Appendix C). We are therefore
confident that the calculations with 512^3 grid points provide sufficiently accurate results.
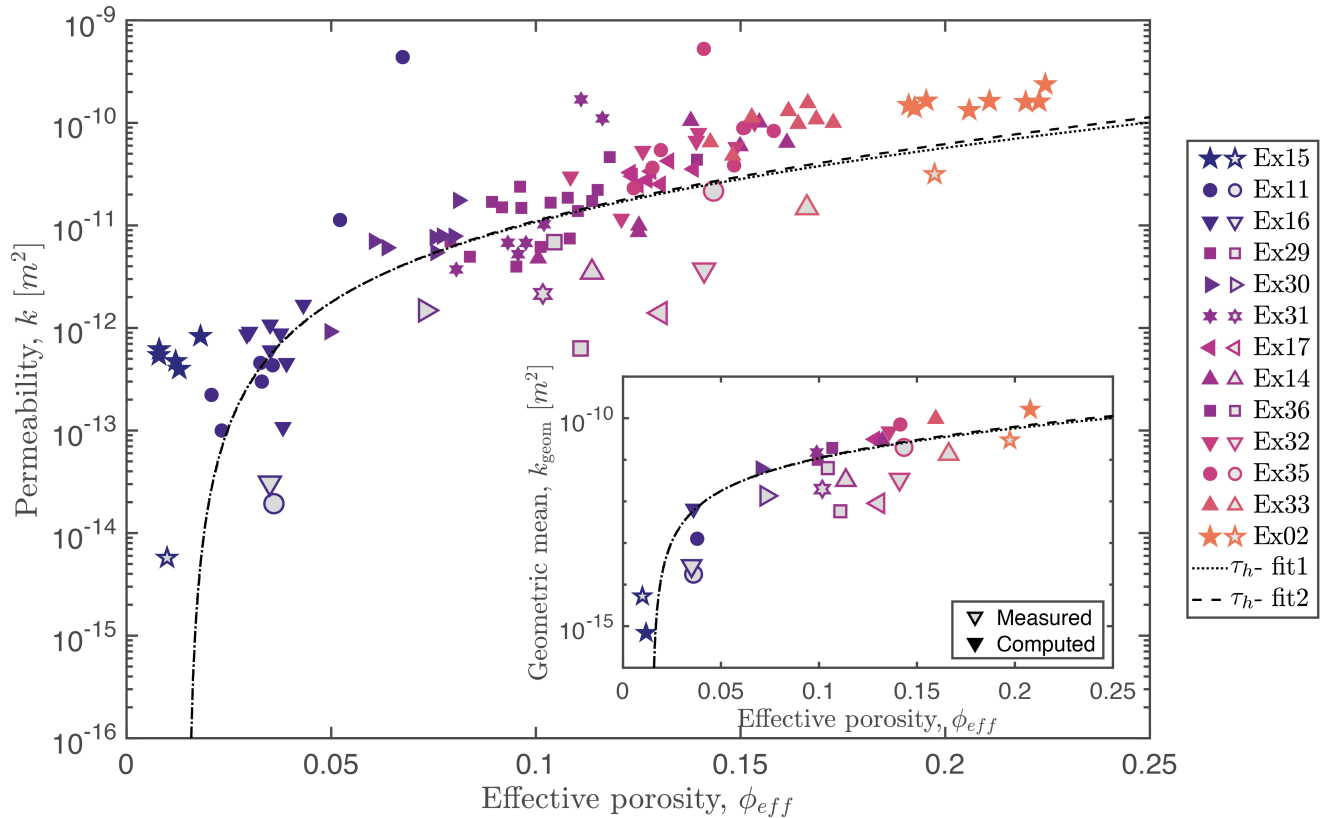
Figure 5. Computed and measured permeability against effective porosity. Symbols of the same shape and color represent the same sample. Samples with grey face color represent measured values, whereas color only symbols stand for computed subsamples. The dotted black line (fit1) represents eq.(25) using the arithmetic mean of computed hydraulic tortuosities, whereas the black dashed line (fit2) shows eq.(24) using the fitted linear curve for hydraulic tortuosity according to eq.(22). The inset displays the geometric mean of the computed hydraulic tortuosities and measured values against effective porosity. Some subsamples with low effective porosity did not show a continuous pathway throughout the subsample, thus we assumed a very low permeability of $10^{-20}\,\mathrm{m}^2$. Note that estimated errors for the experimental permeability measurements (tab.1) are smaller than the displayed symbols.

4 Discussion and conclusion

In this paper, we determine the permeability of nearly isotropic porous media made out of sintered glass beads using a combined
experimental-numerical approach. By analyzing sample microstructures and the flow properties inside these samples, we are
able to derive a modified Kozeny-Carman equation which improves theoretical permeability predictions at low porosities.

The computation of the effective specific surface shows a good fit using eq.(20) from previous studies, not only for the
chosen subsamples but also for the full samples. The computed hydraulic radius of $0.385\,\mathrm{mm}$ is reasonable as the initial grain
size of the glass beads is around $1\,\mathrm{mm}$ and the hydraulic pore radius of the glass beads is reduced during sample sintering.

260   Only few studies have investigated hydraulic tortuosity for three dimensional porous media (Du Plessis and Masliyah, 1991; Ahmadi et al., 2011; Backeberg et al., 2017). In previous studies the hydraulic tortuosity was often assumed or used as fitting parameter as it is challenging to determine, in particular in experimental studies. Our data shows that contrary to suggestions by previous authors the hydraulic tortuosity does not change significantly with decreasing effective porosity (Matyka et al., 2008; Koponen et al., 1996; Mota et al., 2001), at least at the low porosities investigated in this study. We find an increasing

265   scatter towards small effective porosities as the hydraulic tortuosity strongly depends on the sample microstructure. Using two dimensional squares Koponen et al. (1996) found hydraulic tortuosity values close to 2, whereas our data scatters around a value of 3. The difference between previous relations and our data is likely related to the different particle geometries used and that previous studies were done in 2D, while we employ 3D samples.

    Using two dimensional squares the average hydraulic tortuosity of Koponen et al. (1996) is smaller than 2, but in general it

270   displays a similar trend as our data. Our work shows that measured and computed permeability are in good agreement, but the computed permeability tends to yield towards higher values, whereas the measured permeability yields towards lower values in comparison to the permeability prediction using the Kozeny-Carman equation. Differences between numerical and measured permeability might be related to the fact that in order to be able to predict permeability numerically we employ subsamples as computational resources are limited. However, experimental measurements are carried out using the full sample. Thus in

275   terms of permeability some of the subsamples seem not to be representative for the corresponding full sample. Furthermore increasing the numerical resolution affects the computed permeability only by $2-4\%$, demonstrating that subsamples with 512^3 pixels use a satisfactory numerical resolution.

    Our study shows that by determining microstructural parameters the Kozeny-Carman equation can predict permeabilities for isotropic three-dimensional porous media (see eq.(24)). Using the fitted equations for effective specific surface and hydraulic

280   tortuosity we provide a Kozeny-Carman equation for the estimation of permeability as input parameter in large-scale numerical models depending only on porosity. Furthermore predicting permeability for more complex porous media still remains challenging and needs to be investigated in future work.

    This study demonstrates that numerical permeability computations can complement laboratory measurements, in particular in cases of small sample sizes or effective porosities $< 5\%$. Furthermore we provide segmented input files of several samples

285   with different porosities. This should allow other workers to use these input data and our results to benchmark other numerical methods in the future.

Code availability.   https://bitbucket.org/bkaus/lamem/src/master/ ; commit: 9c06e4077439b5492d49d03c27d3a1a5f9b65d32 (Popov and Kaus, 2016).

Data availability.   Detailed data tables to each sample can be found in the supplementary material. The segmented CT images of three

290   samples with different porosities are provided using the figshare repository (doi:10.6084/m9.figshare.11378517).

Appendix A: Applicability of Darcy's Law

For the numerical permeability computation using the Stokes equations we assume laminar flow conditions and incompressibility. Laminar flow conditions are represented by a linear relationship between applied pressure gradient and flow rate (fig.A1). Regarding the incompressibility of the working gas during the measurements we computed permeabilities using both Darcy's

295   law (eq.(1)) and Darcy's law for compressible gas as follows (Takeuchi et al., 2008):

$$\frac{P_2^2 - P_1^2}{2P_2 L} = \frac{\eta \nu_0}{k}, \tag{A1}$$

with P_2 and P_1 being the pressures at the inlet and outlet side of the sample respectively, and ν_0 being the volume flux, which is calculated from the flow rate divided by cross-sectional area of the sample. The left-hand side of Eq.(A1) represents the modified pressure gradient that includes the compressibility of working gas. The difference between both computed permeabilities

300   is less than 10%, we therefore assume the effect of compressibility to be minor.

Appendix B: Grain size distribution of used glass beads
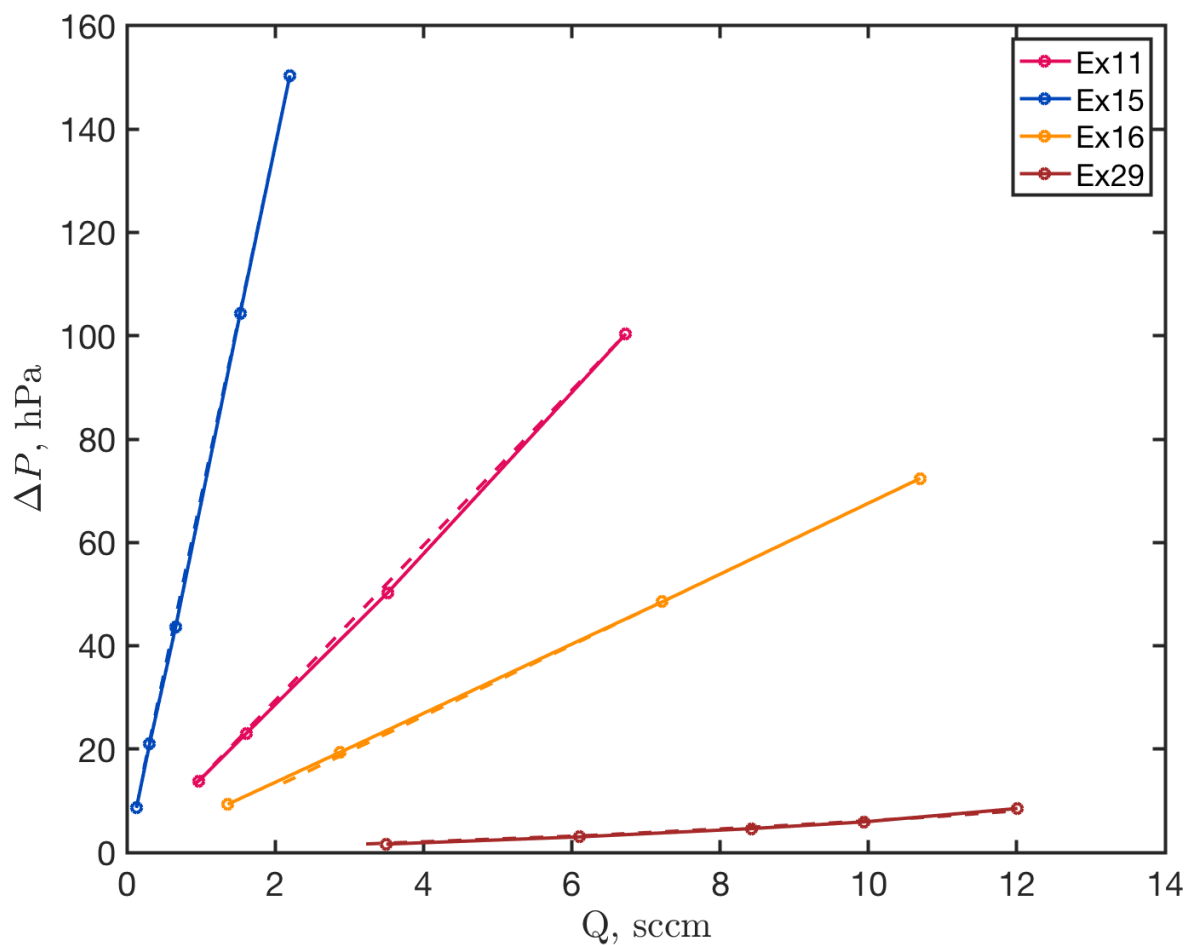
Figure A1. The linear relations between applied pressure and flow rate show that Darcy's law is valid and no turbulent flow occurs. Solid lines represent measurements while increasing the pressure gradient and dashed lines while decreasing the pressure gradient. The unit of *sccm* refers to a standard cubic centimeter per minute.
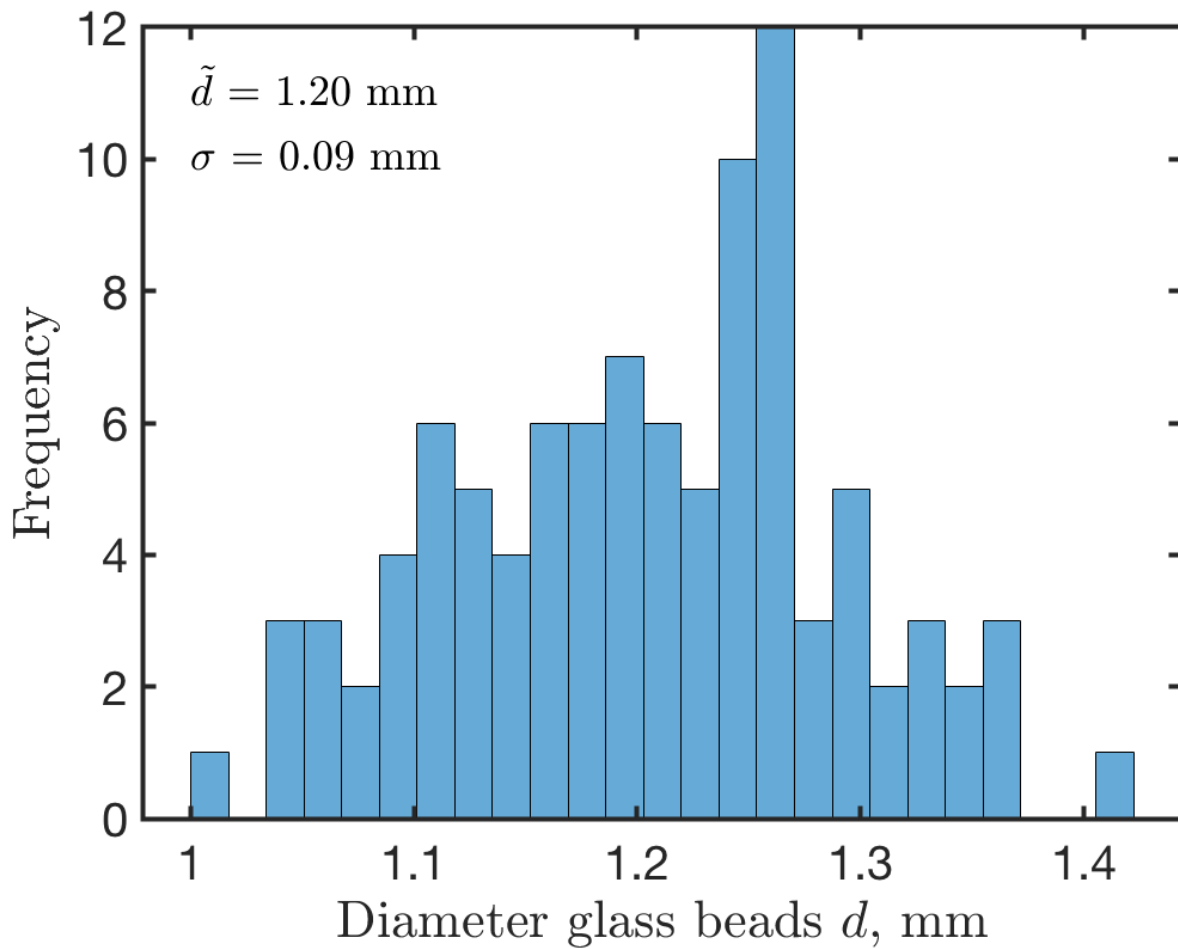
Figure B1. Size frequency distribution of the glass beads diameter. Beside the distribution, both the arithmetic mean $\widetilde{d}$ and standard deviation σ are given.

Appendix C: Resolution test
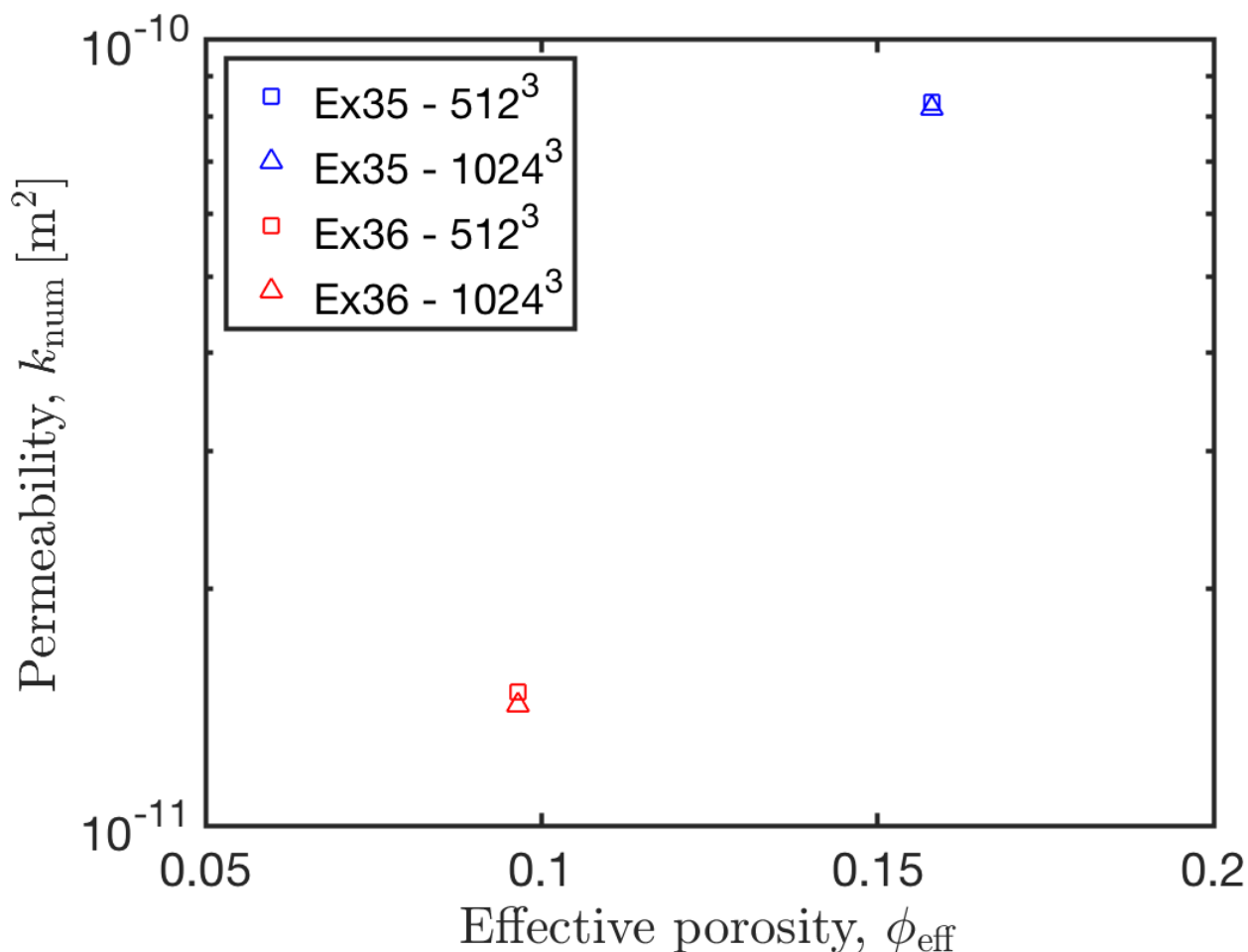
Figure C1. Resolution test using samples Ex35sub04 and Ex36sub02 (for details see also tables in the supplement). Colored squares denote standard resolution of 512^3, whereas colored triangles are simulations with resolution of 1024^3 voxels.

Appendix D: Critical porosity threshold

The samples employed in the present study display a critical porosity threshold of 0.015. In case the spheres are all similarly

305   packed and there should be no critical porosity threshold as the geometrical dihedral angle between the spherical grains and air should be much smaller than $60°$. In the actual experimental products, however, the boundary between the softened soda-lime glass beads started to heal by (i) expelling the air and (ii) element diffusion between the glass beads, resulting in the

decrease of the interfacial tension force and increase of the dihedral angle as observed in the crack healing in supercooled melts (Yoshimura and Nakamura, 2010). This way some pathways are expected to pinch-off and thus form both rugby ball-shaped isolated pockets and cigar-shaped dead-ends (see fig.D1). While the isolated pores were excluded in our calculations, the dead-ends are expected to cause the critical porosity threshold.

310
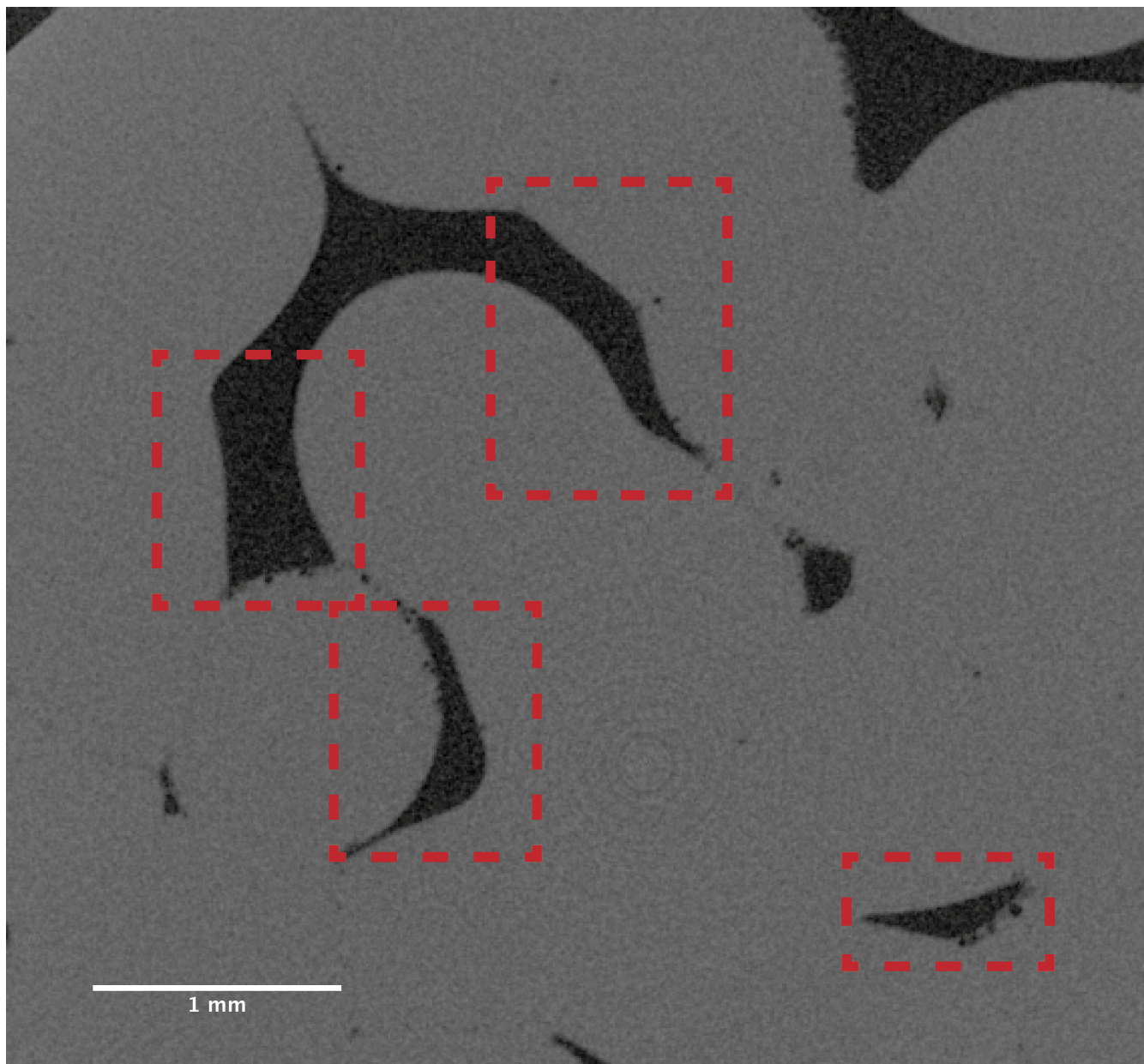
Figure D1. The CT slice highlights several structural features forming the critical porosity threshold.

Author contributions. PE contributed in designing the study, sample preparation and permeability measurement. Futhermore PE did visualization, writing, methodology and running simulations. MT contributed in data interpretation, methodology, designing the study and manuscript writing. WF performed sample preparation and permeability measurements. GJG contributed in designing the study, data inter-

315 pretation and manuscript writing. MN designed the study and contributed in data interpretation. SO contributed in sample preparation and measurement. TK sintered the glass bead porous media. MOK performed the resolution test. All authors contributed in writing and improving the manuscript.

Competing interests. The authors declare that they have no conflict of interest.

Acknowledgements. This work has been supported by DFG (grant no. GRK 2156/1), the JSPS Japanese-German graduate externship and

320 BMBF (grant no. 03G0865A). M.T. was supported by the Bayerisches Geoinstitut Visitors Program. Calculations were performed on clusters btrzx2, University of Bayreuth and Mogon II, Johannes Gutenberg University Mainz.

References

Ahmadi, M. M., Mohammadi, S., and Hayati, A. N.: Analytical derivation of tortuosity and permeability of monosized spheres: A volume averaging approach, Phys. Rev. E, 83, 026 312, https://doi.org/10.1103/PhysRevE.83.026312, 2011.

325 Andrä, H., Combaret, N., Dvorkin, J., Glatt, E., Han, J., Kabel, M., Keehm, Y., Krzikalla, F., Lee, M., Madonna, C., Marsh, M., Mukerji, T., Saenger, E. H., Sain, R., Saxena, N., Ricker, S., Wiegmann, A., and Zhan, X.: Digital rock physics benchmarks—Part I: Imaging and segmentation, Computers & Geosciences, 50, 25 – 32, https://doi.org/doi.org/10.1016/j.cageo.2012.09.005, 2013b.

Andrä, H., Combaret, N., Dvorkin, J., Glatt, E., Han, J., Kabel, M., Keehm, Y., Krzikalla, F., Lee, M., Madonna, C., Marsh, M., Mukerji, T., Saenger, E. H., Sain, R., Saxena, N., Ricker, S., Wiegmann, A., and Zhan, X.: Digital rock physics benchmarks—Part II: Computing
330 effective properties, Computers & Geosciences, 50, 33 – 43, https://doi.org/https://doi.org/10.1016/j.cageo.2012.09.008, 2013a.

Arns, C. H.: A comparison of pore size distributions derived by NMR and X-ray-CT techniques, Physica A: Statistical Mechanics and its Applications, 339, 159–165, https://doi.org/10.1016/j.physa.2004.03.033, 2004.

Arns, C. H., Knackstedt, M. A., Pinczewski, M. V., and Lindquist, W.: Accurate estimation of transport properties from microtomographic images, Geophysical Research Letters, 28, 3361–3364, https://doi.org/10.1029/2001GL012987, 2001.

335 Backeberg, N. R., Lacoviello, F., Rittner, M., Mitchell, T. M., Jones, A. P., Day, R., Wheeler, J., Shearing, P. R., Vermeesch, P., and Striolo, A.: Quantifying the anisotropy and tortuosity of permeable pathways in clay-rich mudstones using models based on X-ray tomography, Scientific Reports, 7, 14 838, https://doi.org/10.1038/s41598-017-14810-1, 2017.

Balay, S., Abhyankar, S., Adams, M. F., Brown, J., Brune, P., Buschelman, K., Dalcin, L., Dener, A., Eijkhout, V., Gropp, W. D., Karpeyev, D., Kaushik, D., Knepley, M. G., May, D. A., McInnes, L. C., Mills, R. T., Munson, T., Rupp, K., Sanan, P., Smith, B. F., Zampini, S.,
340 Zhang, H., and Zhang, H.: PETSc Users Manual, Tech. Rep. ANL-95/11 - Revision 3.12, Argonne National Laboratory, https://www.mcs.anl.gov/petsc, 2019.

Bear, J.: Dynamics of Fluids in Porous Media, Dover Publications Inc., New York, 1988.

Bekins, B. A. and Dreiss, S. J.: A simplified analysis of parameters controlling dewatering in accretionary prisms, Earth and Planetary Science Letters, 109, 275 – 287, https://doi.org/https://doi.org/10.1016/0012-821X(92)90092-A, 1992.

345 Bernabe, Y., Brace, W., and Evans, B.: Permeability, porosity and pore geometry of hot-pressed calcite, Mechanics of Materials, 1, 173 – 183, https://doi.org/https://doi.org/10.1016/0167-6636(82)90010-2, 1982.

Bird, M., Butler, S. L., Hawkes, C., and Kotzer, T.: Numerical modeling of fluid and electrical currents through geometries based on synchrotron X-ray tomographic images of reservoir rocks using Avizo and COMSOL, Computers & Geosciences, 73, 6–16, https://doi.org/10.1016/j.cageo.2014.08.009, 2014.

350 Bird, R., Stewart, W., and Lightfoot, E.: Transport Phenomena, New York, London: Wiley, revised second Edition, 2006.

Bosl, W. J., Dvorkin, J., and Nur, A.: A study of porosity and permeability using a lattice Boltzmann simulation, Geophysical Research Letters, 25, 1475–1478, https://doi.org/10.1029/98GL00859, 1998.

Bourbie, T., Coussy, O., Zinszner, B., and Junger, M. C.: Acoustics of Porous Media, The Journal of the Acoustical Society of America, 91, 3080–3080, 1992.

355 Brace, W. F.: Permeability of crystalline and argillaceous rocks, International Journal of Rock Mechanics and Mining Sciences & Geomechanics Abstracts, 17, 241–251, https://doi.org/10.1016/0148-9062(80)90807-4, 1980.

Carman, P. C.: Fluid flow through granular beds, Trans. Inst. Chem. Eng., 15, 150–166, 1937.

Carman, P. C.: Flow of gases through porous media, New York, Academic Press, 1956.

Clennell, M. B.: Tortuosity: A guide through the maze, Geological Society, London, Special Publications, 122, 299–344, 1997.

360   Collinson, A. and Neuberg, J.: Gas storage, transport and pressure changes in an evolving permeable volcanic edifice, Journal of Volcanology and Geothermal Research, 243-244, 1 – 13, https://doi.org/https://doi.org/10.1016/j.jvolgeores.2012.06.027, 2012.

Comiti, J. and Renaud, M.: A new model for determining mean structure parameters of fixed beds from pressure drop measurements: application to beds packed with parallelepipedal particles, Chemical Engineering Science, 44, 1539 – 1545, https://doi.org/https://doi.org/10.1016/0009-2509(89)80031-4, 1989.

365   Darcy, H. P. G.: Les Fontaines publiques de la ville de Dijon: exposition et application des principes à suivre et des formules à employer dans les questions de distribution d'eau., Paris: V. Dalamont, 1856.

Domenico, P. A. and Schwartz, F. W.: Physical and chemical hydrogeology, Wiley, New York, 1998.

Du Plessis, J. P. and Masliyah, J. H.: Flow through isotropic granular porous media, Transport in Porous Media, 6, 207–221, https://doi.org/10.1007/BF00208950, 1991.

370   Dvorkin, J., Derzhi, N., Diaz, E., and Fang, Q.: Relevance of computational rock physics, Geophysics, 76, E141–E153, https://doi.org/10.1190/geo2010-0352.1, 2011.

Eichheimer, P., Thielmann, M., Popov, A., Golabek, G. J., Fujita, W., Kottwitz, M. O., and Kaus, B. J. P.: Pore-scale permeability prediction for Newtonian and non-Newtonian fluids, Solid Earth, 10, 1717–1731, https://doi.org/10.5194/se-10-1717-2019, 2019.

Fehn, U. and Cathles, L. M.: Hydrothermal convection at slow-spreading mid-ocean ridges, Tectonophysics, 55, 239–260,
375   https://doi.org/10.1016/0040-1951(79)90343-3, 1979.

Gerke, K. M., Vasilyev, R. V., Khirevich, S., Collins, D., Karsanina, M. V., Sizonenko, T. O., Korost, D. V., Lamontagne, S., and Mallants, D.: Finite-difference method Stokes solver (FDMSS) for 3D pore geometries: Software development, validation and case studies, Computers & Geosciences, 114, 41–58, https://doi.org/10.1016/j.cageo.2018.01.005, 2018.

Ghanbarian, B., Hunt, A. G., Ewing, R. P., and Sahimi, M.: Tortuosity in porous media: A critical review, Soil science society of America
380   journal, 77, 1461–1477, 2013.

Harlow, F. H. and Welch, J. E.: Numerical Calculation of Time-Dependent Viscous Incompressible Flow of Fluid with Free Surface, The Physics of Fluids, 8, 2182–2189, https://doi.org/10.1063/1.1761178, 1965.

Hendraningrat, L., Li, S., and Torsæter, O.: A coreflood investigation of nanofluid enhanced oil recovery, Journal of Petroleum Science and Engineering, 111, 128 – 138, https://doi.org/10.1016/j.petrol.2013.07.003, 2013.

385   Hölting, B. and Coldewey, W. G.: Hydrogeology, Springer-Verlag GmbH, Berlin, https://doi.org/10.1007/978-3-662-56375-5, 2019.

Honarpour, M. M.: Relative Permeability Of Petroleum Reservoirs: Boca Raton, Florida, CRC press, 2018.

Kaus, B. J. P., Popov, A. A., Baumann, T. S., Püsök, A. E., Bauville, A., Fernandez, N., and Collignon, M.: Forward and Inverse Modelling of Lithospheric Deformation on Geological Timescales, NIC Series, 48, 299–307, 2016.

Keehm, Y.: Computational rock physics: Transport properties in porous media and applications, Ph.D. thesis, Stanford University, 2003.

390   Koponen, A., Kataja, M., and Timonen, J. v.: Tortuous flow in porous media, Physical Review E, 54, 406–410, https://doi.org/10.1103/PhysRevE.54.406, 1996.

Koponen, A., Kataja, M., and Timonen, J.: Permeability and effective porosity of porous media, Phys. Rev. E, 56, 3319–3325, https://doi.org/10.1103/PhysRevE.56.3319, 1997.

Kozeny, J.: über kapillare Leitung des Wasser im Boden, Royal Academy of Science, Vienna, Proc. Class I, 136, 271–306, 1927.

395   Kuczynski, G. C.: Study of the Sintering of Glass, Journal of Applied Physics, 20, 1160–1163, 1949.

Lamur, A., Kendrick, J. E., Eggertsson, G. H., Wall, R. J., Ashworth, J. D., and Lavallée, Y.: The permeability of fractured rocks in pressurised volcanic and geothermal systems, Scientific Reports, 7, 6173, https://doi.org/10.1038/s41598-017-05460-4, 2017.

Manwart, C., Aaltosalmi, U., Koponen, A., Hilfer, R., and Timonen, J.: Lattice-Boltzmann and finite-difference simulations for the permeability for three-dimensional porous media, Physical Review E, 66, 016 702, https://doi.org/10.1103/PhysRevE.66.016702, 2002.

400 Matyka, M., Khalili, A., and Koza, Z.: Tortuosity-porosity relation in porous media flow, Physical Review E, 78, 026 306, https://doi.org/10.1103/PhysRevE.78.026306, 2008.

Mavko, G. and Nur, A.: The effect of a percolation threshold in the Kozeny-Carman relation, Geophysics, 62, 1480–1482, https://doi.org/10.1190/1.1444251, 1997.

Morais, A. F., Seybold, H., Herrmann, H. J., and Andrade, J. S.: Non-Newtonian Fluid Flow through Three-Dimensional Disordered Porous

405 Media, Phys. Rev. Lett., 103, 194 502, https://doi.org/10.1103/PhysRevLett.103.194502, 2009.

Mostaghimi, P., Blunt, M. J., and Bijeljic, B.: Computations of Absolute Permeability on Micro-CT Images, Mathematical Geosciences, 45, 103–125, https://doi.org/10.1007/s11004-012-9431-4, 2013.

Mota, M., Teixeira, J. A., Bowen, W. R., and Yelshin, A.: Binary spherical particle mixed beds: porosity and permeability relationship measurement, 17, 101–106, 2001.

410 Mueller, S., Melnik, O., Spieler, O., Scheu, B., and Dingwell, D. B.: Permeability and degassing of dome lavas undergoing rapid decompression: An experimental determination, Bulletin of Volcanology, 67, 526–538, https://doi.org/10.1007/s00445-004-0392-4, 2005.

Napolitano, A. and Hawkins, E. G.: Viscosity of a standard soda-lime-silica glass, J. Res. Nat. Bur. Stand. A. A, 68, 439–448, 1964.

Norton, D. and Taylor Jr, H. P.: Quantitative Simulation of the Hydrothermal Systems of Crystallizing Magmas on the Basis of Transport Theory and Oxygen Isotope Data: An analysis of the Skaergaard intrusion, Journal of Petrology, 20, 421–486,

415 https://doi.org/10.1093/petrology/20.3.421, 1979.

Okumura, S. and Sasaki, O.: Permeability reduction of fractured rhyolite in volcanic conduits and its control on eruption cyclicity, Geology, 42, 843–846, https://doi.org/10.1130/G35855.1, 2014.

Okumura, S., Nakamura, M., Takeuchi, S., Tsuchiyama, A., Nakano, T., and Uesugi, K.: Magma deformation may induce non-explosive volcanism via degassing through bubble networks, Earth and Planetary Science Letters, 281, 267 – 274,

420 https://doi.org/https://doi.org/10.1016/j.epsl.2009.02.036, 2009.

Osorno, M., Uribe, D., Ruiz, O. E., and Steeb, H.: Finite difference calculations of permeability in large domains in a wide porosity range, Archive of Applied Mechanics, 85, 1043–1054, https://doi.org/10.1007/s00419-015-1025-4, 2015.

Otsu, N.: A threshold selection method from gray-level histograms, IEEE transactions on systems, man, and cybernetics, 9, 62–66, 1979.

Pape, H., Clauser, C., and Iffland, J.: Permeability prediction for reservoir sandstones and basement rocks based on fractal pore space

425 geometry, pp. 1032–1035, Society of Exploration Geophysicists, https://doi.org/10.1190/1.1820060, 2005.

Pech, D.: Etude de la perméabilité de lits compressibles constitués de copeaux de bois partiellement destructurés, Ph.D. thesis, INP Grenoble, 1984.

Popov, A. and Kaus, B. J. P.: LaMEM (Lithosphere and Mantle Evolution Model), https://bitbucket.org/bkaus/lamem/src/master/, 2016.

Ramandi, H. L., Mostaghimi, P., and Armstrong, R. T.: Digital rock analysis for accurate prediction of fractured media permeability, Journal

430 of Hydrology, 554, 817 – 826, https://doi.org/https://doi.org/10.1016/j.jhydrol.2016.08.029, 2017.

Rintoul, M. D.: Precise determination of the void percolation threshold for two distributions of overlapping spheres, Phys. Rev. E, 62, 68–72, https://doi.org/10.1103/PhysRevE.62.68, 2000.

Saxena, N., Mavko, G., Hofmann, R., and Srisutthiyakorn, N.: Estimating permeability from thin sections without reconstruction: Digital rock study of 3D properties from 2D images, Computers & Geosciences, 102, 79–99, https://doi.org/10.1016/j.cageo.2017.02.014, 2017.

435 Shabro, V., Kelly, S., Torres-Verdín, C., Sepehrnoori, K., and Revil, A.: Pore-scale modeling of electrical resistivity and permeability in FIB-SEM images of organic mudrock, Geophysics, 79, D289–D299, https://doi.org/10.1190/geo2014-0141.1, 2014.

Suleimanov, B. A., Ismailov, F. S., and Veliyev, E. F.: Nanofluid for enhanced oil recovery, Journal of Petroleum Science and Engineering, 78, 431–437, https://doi.org/10.1016/j.petrol.2011.06.014, 2011.

Takeuchi, S., Nakashima, S., and Tomiya, A.: Permeability measurements of natural and experimental volcanic materials with a simple

440 permeameter: toward an understanding of magmatic degassing processes, Journal of Volcanology and Geothermal Research, 177, 329–339, https://doi.org/10.1016/j.jvolgeores.2008.05.010, 2008.

Van der Marck, S. C.: Network Approach to Void Percolation in a Pack of Unequal Spheres, Phys. Rev. Lett., 77, 1785–1788, https://doi.org/10.1103/PhysRevLett.77.1785, 1996.

Wadsworth, F. B., Vasseur, J., von Aulock, F. W., Hess, K.-U., Scheu, B., Lavallée, Y., and Dingwell, D. B.: Nonisothermal viscous sintering

445 of volcanic ash, Journal of Geophysical Research: Solid Earth, 119, 8792–8804, https://doi.org/10.1002/2014JB011453, 2014.

Wadsworth, F. B., Vasseur, J., Scheu, B., Kendrick, J. E., Lavallée, Y., and Dingwell, D. B.: Universal scaling of fluid permeability during volcanic welding and sediment diagenesis, Geology, 44, 219–222, https://doi.org/10.1130/G37559.1, 2016.

Wyllie, M. R. J. and Gregory, A. R.: Fluid Flow through Unconsolidated Porous Aggregates, Industrial & Engineering Chemistry, 47, 1379–1388, https://doi.org/10.1021/ie50547a037, 1955.

450 Yoshimura, S. and Nakamura, M.: Fracture healing in a magma: An experimental approach and implications for volcanic seismicity and degassing, Journal of Geophysical Research: Solid Earth, 115, https://doi.org/10.1029/2009JB000834, 2010.

Zhang, H., Nikolov, A., and Wasan, D.: Enhanced Oil Recovery (EOR) Using Nanoparticle Dispersions: Underlying Mechanism and Imbibition Experiments, Energy & Fuels, 28, 3002–3009, https://doi.org/10.1021/ef500272r, 2014.